Vol. 2, No. 2 Journal of Energy Science and Technology April, 2023
第 2 卷第 2 期 能源科学与技术 2023 年 4 月

Co-Ni Bimetallic Sulfides Functionalized Interlayer with Efficient Catalytic Conversion for Li-S Batteries

Hongqiang Wang, Zhijie Zhang, Liyuan Shen, Juantao Jiang, Qingyu Li, Yezheng Cai, Zhaoling Ma[*]

Guangxi Key Laboratory of Low Carbon Energy Materials, Guangxi New Energy Ship Battery Engineering Technology Research Center, Guangxi Scientific, and Technological Achievements Transformation Pilot Research Base of Electrochemical Energy Materials and Devices, School of Chemistry and Pharmaceutical Sciences, Guangxi Normal University, Guilin 541004, China

Abstract: Tardive practical development of lithium-sulfur (Li-S) batteries faces two fatal nuisances, the grievous shuttle effect of sulfur electrodes as well as rock-ribbed Li dendrites, which results in undesired cycling lifespan and the potential safety hazard. Diversified electrocatalytic materials are employed to enhance polysulfides conversion kinetics and subsequently restrain shuttle effect. Here, pyrite-type cation regulation strategy is applied to motivate the electrochemical catalysis capability of bimetallic sulfide by regulating the cation ratio of Co and Ni ions. The reformative bimetallic sulfide with Co to Ni ratio near 2:1 shows stronger chemical adsorption capability towards lithium polysulfides in contrast to pristine NiS_2, which resulted from the strong contribution of metal oxide layer. The comparable electrochemical kinetics and electrochemical performances of Li-S batteries with CNS-2/CP interlayer show in the aspects of low polarization voltage, high lithium ion diffusion rate, high discharge capacity, as well as better rate performances. These results demonstrate cation regulation could be an efficient strategy for material design to optimize the surface physicochemical properties of iron pyrite for boosting the cycle durability of Li-S batteries.

Keywords: Li-S Batteries; Lithium Polysulfides; Catalytic Conversion; Functionalized Interlayer; Bimetallic Sulfide

DOI: 10.57237/j.jest.2023.02.001

1 Introduction

Compared with the present commercial lithium ion batteries, lithium-sulfur (Li-S) batteries possess the intrinsic superiority of high energy density (~2600 Wh kg^{-1}) and extraordinary specific capacity (1672 mAh g^{-1}) [1, 2]. However, the practical application of Li-S batteries still tolerate several drawbacks: (I) low sulfur content in the composite of sulfur/carbon; (II) low areal mass loading in the sulfur electrode; (III) low sulfur utilization; (IV) high electrolyte usage amount [3-5]. The most critical issue of the low sulfur utilization originates from the feature of the used ether-based electrolyte enjoying dissolving lithium polysulfides (LiPSs) (Li_2S_x, $4 \le x \le 8$) [6] and the inherent slow kinetics of polysulfides conversion reaction [7]. However, the usage of the ether-based electrolyte is still a

---

Funding: National Natural Science Foundation of China (22002025);
Guangxi Natural Science Foundation (2021GXNSFAA075040, 2021GXNSFBA220078);
Guangxi Technology Base and Talent Subject (GUIKE AD18126001, GUIKE AD19110119, GUIKE AD19110028).

[*] Corresponding author: Zhaoling Ma, zhaolingma@163.com

Received: October 28, 2022; Accepted: March 7, 2023; Published Online: March 28, 2023

desired electrolyte because it could prompt the generated lithium polysulfide loss in the discharging and storage process. In addition, those cause the grievous consumption of Li anode and deteriorate the discharge capacity and cycle life. In fact, the dissolved liquid polysulfides avail the promotion of kinetics to a certain extent and its subsequent migration is mainly on account of the unappeasable kinetics [8]. Therefore, the slow kinetics of polysulfides conversion of ether electrolyte based Li-S batteries should be given more considerable attentions.

Highly efficient electrocatalytic materials including three main types of heteroatom doped carbon, single atom metal, and polar transition metal compounds [9-12], are implanted on the conductive supporters for boosting the kinetics of polysulfides conversion. The synergistic collaboration of strong chemical adsorption and rapid redox conversion towards lithium polysulfides ($Li_2S_n^{2-}$, LiPS) has been testified and focused vast attraction. Among electrocatalytic materials for Li-S batteries, transition metal sulfides with good electrical conductivity, easily tunable merit for structure, and available electrocatalytic effect were often employed to be as the sulfur host and the separator decoration [10]. Metal sulfides enable binding with LiPSs to form $M^{\delta+}$-S_n^{2-} and $S^{\delta-}$-Li^+ bonds via Lewis acid base interaction along with a pathway for the subsequent rapid transport of electrons and ions [13, 14].

Especially, pyrite-type transition metal sulfides such as CoS_2, NiS_2, FeS_2 used in Li-S batteries have unique chemical adsorption and electrocatalytic capability for polysulfides. The pivotal role in HER and OER along with the remarkable electrocatalysis performances certified their important value in accelerating oxidation and reduction reaction [15]. pyrite-type transition metal sulfides possess the metallic conductivity, such as 50 S cm^{-1} for CoS_2, 55 S cm^{-1} for NiS_2 and 50 S cm^{-1} for FeS_2 [16]. That would provide more rapid electron transport pathways for the electrocatalytic conversion of polysulfides. Moreover, it was found that CoS_2 outclassed NiS_2 in the aspects of improving conversion and redox kinetics of polysulfides, binding lithium polysulfides, and promoting the Li^+ diffusion [17]. In consideration of the above preponderances, we were inclined to regulate cation ratio and implant Ni elements into CoS_2 crystal structure for the purpose of improving its electrocatalytic effect and ultimately prolonging the cycle life of Li-S batteries.

The electrocatalytic materials functionalized separator centralized separation effect and catalytic effect toward polysulfides [18]. It can effectively promote reaction kinetics of polysulfides conversion and then retarded polysulfide shuttle. Our previous work on Co-Fe bimetallic sulfide functionalized separator has verified the brilliant electrocatalysis capability of bimetallic pyrite [19]. Here, we adopted cation regulation strategy and developed Co-Ni sulfides (CNS) electrocatalytic material by a facile hydrothermal method. CNS grown on carbon paper (CP) was used to functionalize the conventional separator in Li-S battery. Such design owns the following merits: (i) the interconnected macropores and mesopores of CP not only act as an electrolyte buffer reservoir to shorten mass diffusion distance but also facilitate fast mass transport ensuring high cycling performance, (ii) smaller CNS nanoparticles exposed more electrocatalytic area, (iii) Optimized combination of bimetal cations could regulate the surface polarity and change the electron structure even the electrocatalytic behavior towards polysulfides conversion.

2 Method

2.1 Preparation of Bulk NiS_2 and CNS Powder

Bulk NiS_2 was prepared by one step hydrothermal synthesis. 1.0 mM $NiCl_2$ $6H_2O$ and 1.2 mM $Na_2S_2O_3$ $5H_2O$ were dissolved in 60 ml glycol/deionized water (volume ratio 3:1) mixture solvent. After stirring for 5 min, the solution was transferred into a 100 ml Teflon-lined stainless-steel autoclave and maintained at 180 ℃ for 12 h. The final product was obtained by washing with deionized water several times, and then dried at 60 ℃ for 12 h. CNSs were prepared in the same way but with different molar ratio of metal salts. The samples with $CoCl_2$ $6H_2O$ and $NiCl_2$ $6H_2O$ of 2:1 and 1:1 were respectively denoted as CNS-2 and CNS-1.

2.2 Preparation of CNS-2/CP Interlayer

CNS-2/CP interlayer was prepared by growing CNS-2 on the commercial CP with a thickness of 0.3 mm (Toray, Japan). Prior to use, CP was calcined at 400 ℃ for 16 h in air to remove impurities as well as improve its surface hydrophilic. After that, the mixed solution of 45 ml glycol and 15 ml deionized water was added $CoCl_2$ $6H_2O$, $NiCl_2$ $6H_2O$ and $Na_2S_2O_3$ $5H_2O$ with the molar ratio of

2:1:3 and sealed in a Teflon-lined stainless-steel autoclave. The treated CP was subsequently added into the above solution and underwent the hydrothermal process at 180℃ for 12 h together. CNS-2/CP was obtained after washing with deionized water and then dried at 60℃ for 12 h. For investigating the effect of mixture solvent on the morphologies of CNS-2/CP, different solvent ratios of glycol and deionized water with 1:3, 1:1, 3:1 were used to prepare CNS-2/CPs. A series of cobalt source concentration were used to inspect the loading of CNS-2 on CP for obtaining enough electrocatalysis.

2.3 Preparation of S/rGO Composite

S/rGO composite was prepared to act as the active material in the sulfur electrode. Graphite oxide was first prepared by the Hummers method as in the previous articles. Graphene oxide solution was obtained by ultrasonicating graphite oxide in water. Reduced graphene oxide (rGO) was obtained by thermally reducing the dried graphene oxide in a tube furnace at 800℃ for 2 h under Ar protection. Sublime sulfur and rGO were mixed with a weight ratio of 9:1 and carried out a conventional melt-impregnate strategy to get S/rGO composite.

2.4 Preparation of Lithium Polysulfide and the Corresponding Adsorptions Test

10 mM Li_2S_6 solution was prepared by dissolving Li_2S and sublimed sulfur (molar ratio = 1:5) in the mixture solvent of dimethoxyethane (DME) and 1,3-dioxolane (DOL) (volume ratio =1:1). The colorless solution gradually changed into saffron yellow under heating and stirring in the glovebox. The adsorptions test of samples (CNS-2, CNS-1 and NiS_2) was executed with the same quality of 60 mg. In order to verify the adsorption capacity, the pristine Li_2S_6 solution and the solutions after the adsorptions test were implemented for the determination of UV-Vis spectrum.

2.5 Materials Characterization

The crystal structure of samples were characterized by X-ray diffraction (Rigaku D/max 2500V/PC, Cu Kα radiation, 30 KV). Thermogravimetric Analysis (TGA) of S/rGO composite was accomplished on Jupiter STA 449 F3 at a heating rate of 5℃ min^{-1} under Ar atmosphere. The morphology and microstructure characterization of samples were carried out with a field-emission scanning electron microscope (FESEM, FEI Quanta 200 FEG), a high-resolution transmission electron microscope (HRTEM, JEOL 2100F). X-ray photoelectron spectra (XPS) measurements were carried out by a K-$Alpha^+$ (Al Kα radiation, America) to probe the oxidation states of elements on the surface. All peak values were revised by the characteristic peak of C 1s at 284.6 eV.

2.6 Cell Assembly and Electrochemical Measurements

To measure the electrochemical performances, the active materials were prepared into the electrode and assembled into the coin-type cells. The active materials, Super P and LA133 were mixed at the mass ratio of 72:20:8 in the mixture solvent of N-propanol and deionized water (volume ratio = 3:1) to form the slurry, and then coated on copper foil as the cathode electrodes. CR2032 coin cells were assembled in an Ar filled glovebox (Mikrouna Super 1220/750). Lithium foil and Celgard 2400 were used as anode and separator. 1M bis(trifluoroethanesulfony)imide lithium (LiTFSI) was dissolved in a mixture solvent of DME and DOL (1:1, v/v) with 1%wt $LiNO_3$ as the electrolyte.

Cyclic voltammetry (CV) measurement and electrochemical impedance spectroscopy were carried out on an electrochemical workstation (CHI 660E). Galvanostatic charge/discharge tests were carried out with a cut-off voltage of 1.7-2.8 V versus Li/Li^+. UV-vis spectra of lithium polysulfides were executed with the wavelength range of 300-800 nm.

3 Results and Discussion

In solvothermal synthesis process, we explored the effects of the mixture solvent constitution on the morphologies of CNS-2/CPs and the effect of cobalt source concentration on the loading mass of CNS-2 on CP. The mixture solvent constitution with glycol and H_2O were adjusted from 1:3 to 3:1. It was affirmed that CNS-2 particles have homogeneous nanoscale size when glycol was increased to 75% volume fraction (3:1 for glycol and H_2O) as shown in Figure 1. Further investigation was executed on the cobalt source concentration effect on the loading mass of CNS-2 on CP in Figure 2. It was observed that with the progressive increase of cobalt source concentration, the grown CNS-2 nanoparticles gradually and integrally occupied on the surface CP until the condition of 1.0 mM cobalt source. The obtained uniform electrocatalyst layer is beneficial for offering enough catalytic area to boost polysulfide conversion.

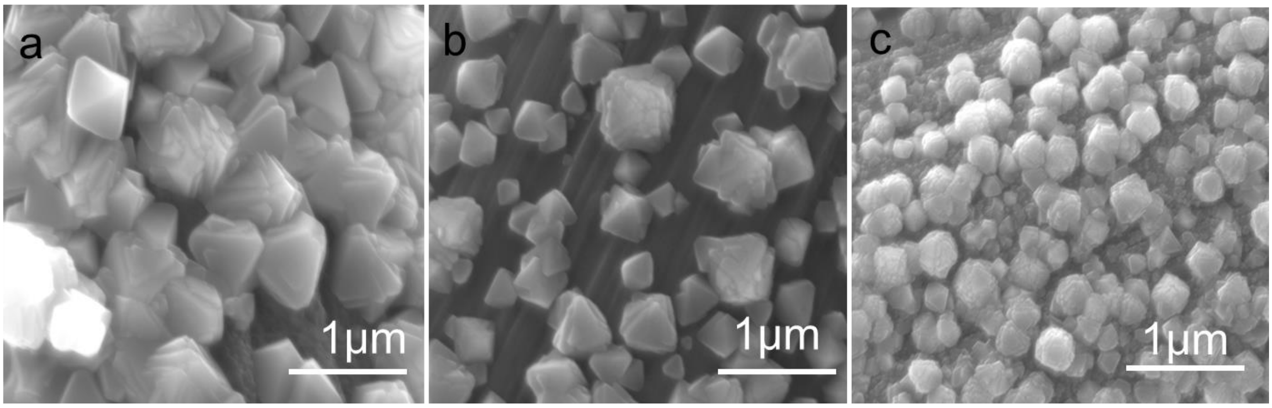

Figure 1 The SEM images of CNS-2/CPs prepared at the mixture solvent of glycol and H_2O with ratio of 1:3 (a), 1:1 (b), 3:1 (c)

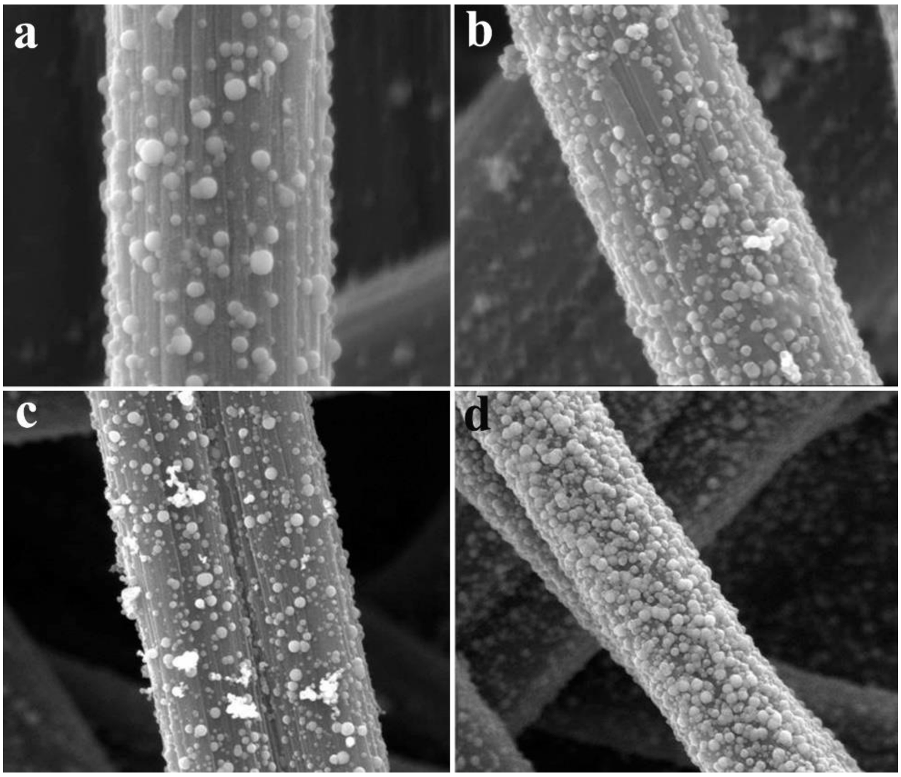

Figure 2 The SEM images of CNS-2/CPs prepared under different cobalt source concentration of (a) 0.3 mM, (b) 0.6 mM, (c) 0.8 mM, (d) 1.0 mM with 3:1 molar ratio of cobalt source to nickel source

In attempt to comprehend the profound significance of adjusting bimetallic ratio, CNS-2, CNS-1 and NiS_2 powders were initially synthesized at the above synthesis condition except for modulating the ratios of cobalt source and nickel source as 2, 1, 0. Further polysulfide-trapping tests for Li_2S_6 as the representative of lithium polysulfides with six or more S atoms were conducted due to its severe corrosion towards Li anode [20]. Same amounts of NiS_2, CNS-1 and CNS-2 powders were added into 2 ml of 3 mM Li_2S_6 as shown in the insert of Figure 3a. It was clearly found that the color of CNS-2 vial turned almost transparent in contrast to the slight adsorption for CNS-1 and almost no adsorption for NiS_2, indicating strong chemical binding capability of CNS-2 towards polysulfides and robust inhibiting capability for Li anode persecution [21]. Simultaneously, UV-vis spectroscopies were utilized to accurately detect the concentration of Li_2S_6 solutions before and after chemical adsorption. Obviously, all the above four materials have absorption capacity for Li_2S_6 solution due to the lower absorbance peak intensities of near to 400 nm. The absorption capacity order is CNS-2> CNS-1> NiS_2.

Figure 3b further gives the XRD pattern of CNS-2/CP whose characteristic peaks are between the counterparts of CoS_2 (JCPDF card No. 41-1471) and NiS_2 (JCPDF card No. 11-0099) and the peak position is more closed to CoS_2, suggesting the congeneric pyrite-type structure and more CoS_2 chemical component. As shown in Figure 3c, CNS-2 particles with the nanoscale size around 300-600 nm were well-distributed on CP, which could expose more catalytic sites to interact with LiPS. The capillary adsorption force from the spindly channels constructed by the interconnected macropores and mesopores are considered as the strong physical trap until now. Choosing CP as the supporter of electrocatalyst could provide a buffer reservoir for polysulfide migration ensuring high utilization of active S and better cycling performance [22-24]. Energy-dispersive X-ray spectroscopy (EDS) under SEM mode of Figure 3d showed Co, Ni and S elements and their element ratio of near to 2:1.

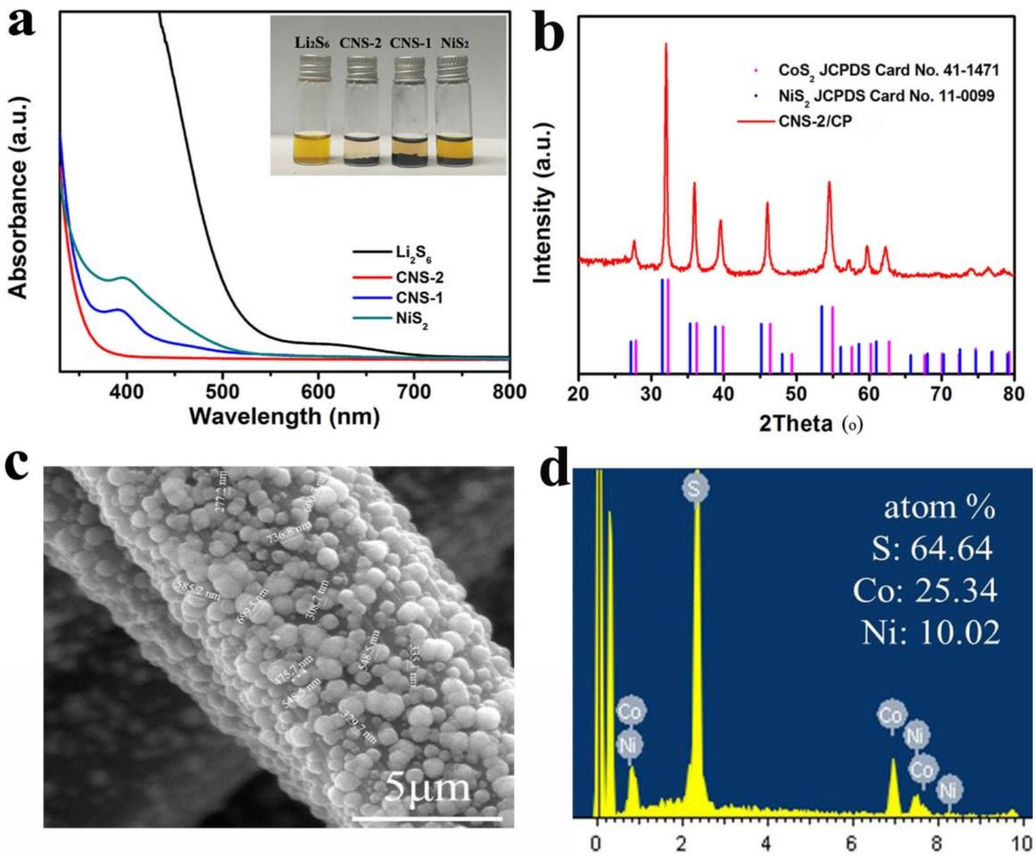

Figure 3 (a) UV-vis spectra and the corresponding chemical adsorption tests of the Li_2S_6 solution with CNS-2, CNS-1 and NiS_2. (b) The XRD pattern, (c) SEM image and (d) EDS image of CNS-2/CP

The inner crystal structure of CNS-2/CP and surface chemical environment were further characterized and analyzed by transmission electron microscopy (TEM), EDS element mapping and XPS. Figure 4a exhibits rough and irregular surface of CNS-2 spherical particle and seems smaller accumulation granule along with hierarchical crystallinity. Interestingly, the element mapping of Figure 4b-d CNS-2 particle core concentrated more Ni element, its external rim occupied more Co element, and S element was uniformly incorporated. That suggested that the outlayer of CNS-2 particle distributed more Co cations in contrasted to Ni cations. Further HRTEM image of Figure 4e showed reconstructed CNS-2 particles with the d-spacing of 0.325 nm and 0.28 nm between (111) and (200) planes of CoS_2 and NiS_2. This result corresponded to that of XRD and further demonstrated the prepared CNS-2 particle with sole crystal texture.

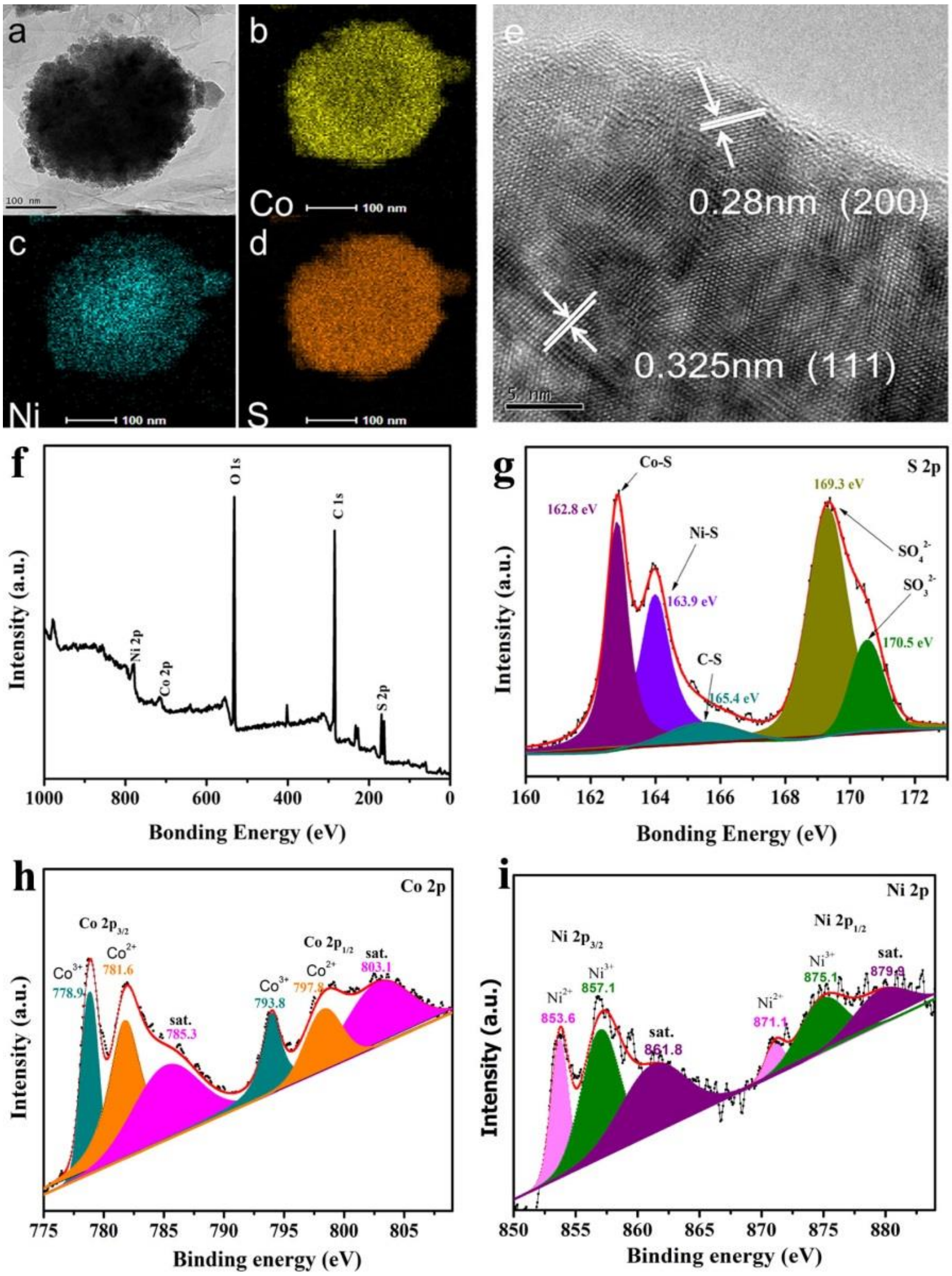

Figure 4 (a-e) TEM, EDS and HRTEM of CNS-2/CP. (b-d) Element dispersion mapping of CNS-2/CP. (f-i) XPS survey spectrum and the corresponding (b) S 2p, (c) Co 2p, (d) Ni 2p spectra of the CNS-2/CP

XPS analysis was used to deeply identify the accurate surface composition of the as-prepared CNS-2/CP. Figure 4f revealed the excepted C, Co, Ni and S elements. The emerging signal of O is possibly described as natural surface oxidation of CNS-2/CP. The In S 2p spectrum of Figure 4g, the peaks at 162.8 eV and 163.9 eV are respectively ascribed to the Co-S and Ni-S bonds [25-27]. The peak at 165.4 eV belongs to C-S bond, implying the strong fastness of CNS-2 to CP substrate. The other two peaks at 169.3 and 170.5 eV ave belonged to SO_4^{2-}or SO_3^{2-} [28]. As for Co 2p spectrum of Figure 4h, two peaks at 778.9 eV and 793.8 eV are attributed to Co^{3+}. The other two peaks at 781.6 eV and 797.8 eV are recognized as Co^{2+} [29]. Two satellite peaks at 785.3 eV and 803.1 eV are observed. The above results indicated the coexistence of both Co^{2+} and Co^{3+} and the mildly oxidized surface focusing more Co^{3+}. Figure 4i showed the Ni 2p spectrum, where the peaks at 853.6 eV and

871.1 eV correspond to Ni^{2+} [30]. The peaks at 857.1 eV and 875.1 eV are ascribed to Ni^{3+} [31], similarly suggesting mixed ion coexistence. The peaks at 861.8 eV and 879.9 eV are belonged to two shake-up satellites [32]. The mixed ion coexistence and the emerged signal of O implied the oxidation of metal ions and the formation of Co-O and Ni-O bonds, which is beneficial for retarding wanton migration of polysulfides and wicked Li anode corrosion [33-37].

S/rGO composites were used as active material to prepare cathode and then assembled Li-S batteries respectively with CNS-2/CP and CP interlayers. CV are measured at a low scan rate of 0.1 mV s^{-1} with a potential window of 1.7-2.8 V versus Li/Li^+ to validate the electrocatalytic effect. The current density is normalized by the quantity of sulfur in rGO/S cathode as shown in Figure 5a. Obvious two reduction peaks and one overlapped oxidation peak display the electrochemical conversion among S_8, long-chain Li_2S_x ($4 \le x \le 8$) and short-chain insoluble Li_2S_2/Li_2S. Further observation found that the utilization of CNS-2/CP interlayer could afford the decreased polarization voltage from 0.38 V to 0.35 V, which implied increased electron transport capability [38, 39]. Based on CV measurements, electrochemical kinetics of polysulfides conversion at charge and discharge processes were evaluated by the corresponding Tafel plots. Both Figure 5b and 5c show that the CNS-2 modified layer on CNS-2/CP interlayer gives lower Tafel slopes explaining effective enhanced oxidation and reduction kinetics for polysulfides conversion and the subsequent remission of the terrible polysulfide shuttle [40, 41]. On the other hand, it is an identified fact that CNS-2/CP interlayer boost oxidation kinetics for polysulfides beyond reduction kinetics. That implies CNS/CP is more inclined to expedite the electrochemical catalysis of Li_2S to S.

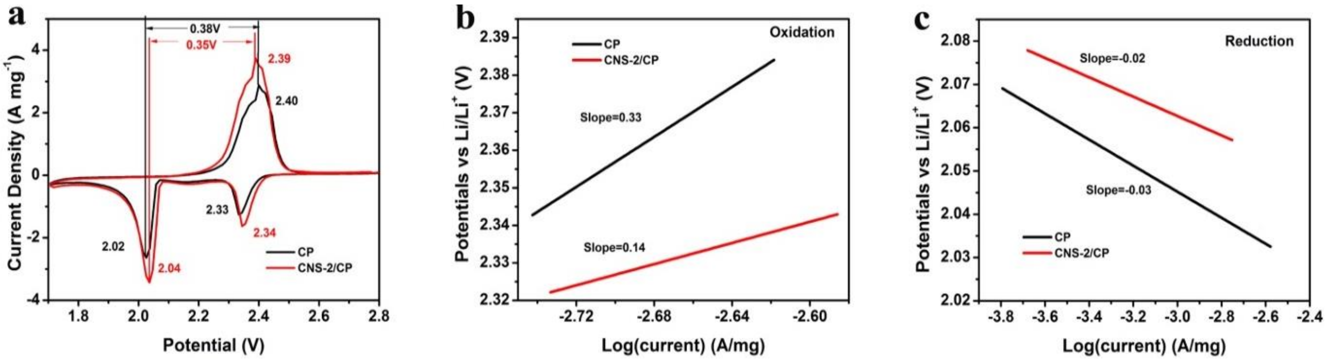

Figure 5 (a) CV plots and (b-c) Tafel plots of Li-S batteries with CNS-2/CP and CP interlayers

To gain better understanding of the contribution of CNS-2/CP interlayer on improving electron migration and lithium ion diffusion, electrochemical impedance spectroscopy (EIS) was carried out from 100 kHz to 0.01 Hz. The corresponding Nyquist plots are shown in Figure 6a. Two Li-S batteries exhibit distinct semicircles in high frequency region and a straight line in low frequency region, which are related to charge transfer resistance (R_{ct}) and lithium ion diffusion process. Li-S battery with CNS-2/CP interlayer gives lower R_{ct} value of 22.1 Ω versus 29.4 Ω of bare CP interlayer, signifying the faster electron transport. The evaluation of lithium ion diffusion coefficients was advantageously access to the kinetics magnitude of polysulfides conversion in Li-S batteries. According to Nyquist plots, we got the diagram of Z' versus $\omega^{-1/2}$ in Figure 6b. Lithium ion diffusion coefficients were evaluated based on the following equation:

$$D_{Li}{}^{+}=R^2T^2/2S^2n^2F^4C^2\sigma^2$$

Typically, R and T are the gas constant and absolute temperature, respectively. S is the electrode area. n is the number of electrons involved in the redox process. C is the shuttle concentration. F is the Faraday constant and σ is the Warburg factor. Thence, the diffusion coefficients are only related to Warburg factor, which can be obtained from the diagram of Z' versus $\omega^{-1/2}$. The linear equation slope is according to σ. It is clear that CNS-2/CP interlayer has a lower slope compared to CP interlayer, simultaneously exhibiting four times the lithium ion diffusion coefficients in contrast to bare CP. It is believed that CNS-2 particles decrease inner resistance and offer fluent conductive pathways for the transport of electron and Li^+, profiting from the fast conversion of lithium polysulfides [42, 43].

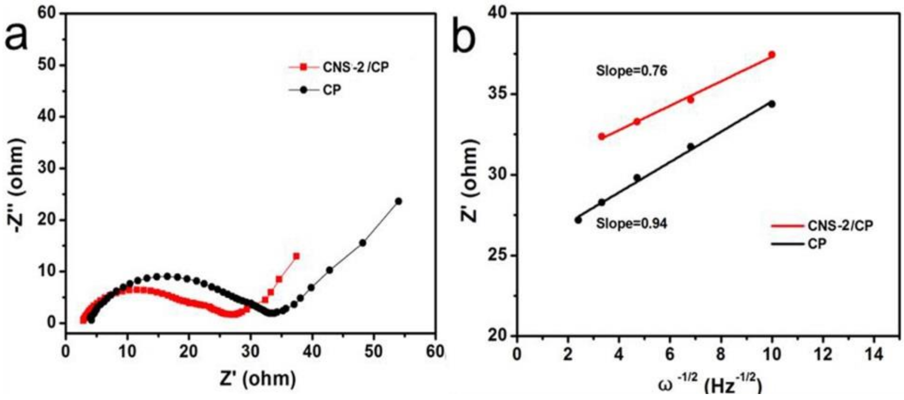

Figure 6 (a) Nyquist plots of impedance measurements and (b) Fitted straight lines of Z' vs. $\omega^{-1/2}$ at low frequency of Li-S batteries with CNS-2/CP and CP interlayers

To inspect rate performances, CNS/CP interlayer was integrated into Li-S batteries as catalytic interlayer and subject to galvanostatic discharge-charge cycling at different current densities. All specific capacities were normalized to the mass of sulfur in cathode. TGA of Figure 7a gives the result of 71.8% sulfur in S/rGO composite. Rate performances of Figure 7b show that rGO/S electrode with CNS-2/CP interlayer delivers the higher capacity at each discharge rate than with bare CP. Moreover, with CNS-2/CP interlayer, S/rGO electrode shows superior rate performances than with especially at high rates of 0.5C and 1C. It is clear that the initial discharge capacity of 1414.4 mAh g^{-1} at 0.1C for CNS-2/CP interlayer outclasses 1213.3 mAh g^{-1} of CP interlayer. Even at 0.5C and 1C, CNS-2/CP interlayer still respectively achieve better specific capacities of 961.6 mAh g^{-1} and 847.9 mAh g^{-1}. When back to 0.1C, a discharge capacity of 1142 mAh g^{-1} was retained corresponding to a high capacity retention of 93.3%.

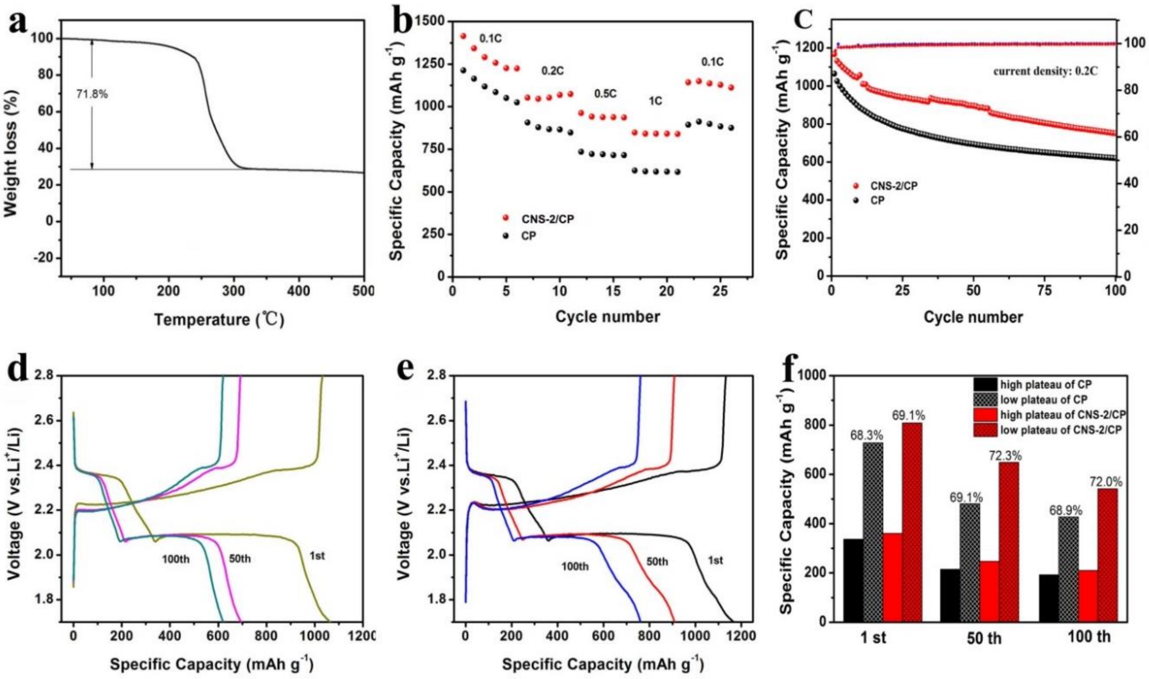

Figure 7 (a) Sulfur content of S/rGO composite. (b) Galvanostatic test at different current density from 0.1C to 1C of S/rGO electrodes with CNS-2/CP and CP interlayers. (c) Cycle performances of S/rGO electrodes with CNS-2/CP and CP interlayers at 0.2C. Charge/discharge voltage profiles of S/rGO electrodes with CP (d) and CNS-2/CP interlayers (e). (f) Discharge specific capacities comparisons on high and low voltage plateaus at 0.2C

Table 1 Performances comparison of Li-S batteries

Cathode/interlayer	**S content**	**Initial discharge capacity/ mAh g^{-1}**	**Capacity retention /mAh g^{-1}**	**Ref.**
CNS/CP	71.8%	1167.2	751.2 (100)	This work
$Ni_xCo_{3-x}S_4$/N-doped carbon hybrid	-	1608 (0.2C)	532 (400)	[44]
S/$NiCo_2S_4$@CT	75%	1600 (0.1C)	836 (500)	[45]
$FeCo_2S_4$/CC	-	969 (0.5 C)	729 (300)	[46]
NiCoP	80%	815.3 (0.1C)	620.1 (250)	[47]
$NiCo_2S_4$	69.5%	600 (0.5 C)	318.9 (500)	[48]
NiCoS/PP	-	1041 (0.2C)	573 (500)	[49]
Ni-foam@$NiCo_2S_4$	-	808.61 (0.5 C)	490.03 (150)	[50]
$NiCo_2O_4$	75%	1171 (1 C)	487 (1500)	[51]
PNS-$Ni_2Co_4P_3$	-	1051 (1 C)	658 (1000)	[52]
Ni_3FeN/G	-	900 (0.5 C)	801 (150)	[53]
NiCo-DH	85.2%	1348.1 (0.1C)	675.6 (1500)	[54]
Ni/Fe LDH	70%	1091 (0.2 C)	724.5 (200)	[55]
MgAl-LDH	55%	1375 (0.1 C)	300 (200)	[56]
SnS_2/TiO_2	55.2%	1140 (0.2 C)	739 (100)	[57]
WS_2@Co_9S_8	49.36%	600 (2 C)	800 (1000)	[58]
$NiCo_2S_4$	-	981 (0.2C)	477.5 (800)	[59]
NiAl@PAB/S	66	1216.3 (0.2C)	473 (300)	[60]

The electrodes were cycled under a constant current density of 0.2C to investigate the long-term cycling stability (Figure 7c). The CNS-2/CP interlayer has higher specific capacity of 1167.2 mAhg^{-1} compared to 1065 mAhg^{-1} of CP interlayer. In the subsequent 100 cycles, it holds lower capacity decay rate until to the specific capacity of 751.2 mAh g^{-1}, whose capacity performance is comparable with other bimetallic oxides, bimetallic sulfides and metal compound hybrids as shown in Table 1. CNS-2/CP interlayer exhibits much higher discharging/charging stability than CP interlayer, due to the existence of CNS-2 particles that can effectively prevent LiPs from “shuttling” to Li anode. The higher specific capacity and lower capacity decay rate are caused by the feature that CNS-2/CP can not only trap sulfur species, but can also provide more electrocatalytic active sites. The discharging/charging curves of CNS-2/CP and CP electrode at 0.2C (1 C =1675 mAh g^{-1}) are shown in Figure 7d and 7e, where the three pairs of discharging/charging curves from right to left are corresponding to the 1st, 50th and 100th cycles. And there are two discharge voltage plateaus at around 2.0 V and 2.3 V and lower voltage difference is consistent with the result from CVs. Further discharge specific capacities comparisons on high and low voltage plateaus were made between CNS-2/CP and CP interlayers. The results intuitively demonstrate CNS-2/CP interlayer has higher capacities on two voltage plateaus. Besides, the zealous role of CNS-2/CP interlayer enables the capacity contribution ratio of low plateau to be boosted from 69.1% to 72%, more near to 75% of the capacity contribution [61]. That is ascribed to the vivacious catalytic effect of CNS-2 making for the keen interception and speedy conversion of lithium polysulfides.

Li-S cells are disassembled after 100 cycles at 0.2C, and then CNS-2/CP interlayer is taken out for further exploration. Observing SEM images in Figure 8a and b of CNS-2/CP interlayer after cycling, it is clear that the surface of CNS-2/CP was covered with the dissolved polysulfides, but the nanoparticle shape and size were as same as the pristine one. The chemical constituent identification was further performed by EDS of Figure 8c. The element ratio of Co, Ni and S remained basically the same before cycling, which further demonstrated the eminent electrochemical stability of CNS-2/CP. That contributes to the continuous and efficacious electrocatalysis behavior of CNS-2/CP interlayer towards LiPs. Schematic illustration of suppression “shuttle effect” with CNS-2/CP separator, as seen in Figure 8d. Co-Ni bimetallic sulfides functionalized interlayer expedited the bidirectional transformation of S and Li_2S and sustained comparable electrochemical performances.

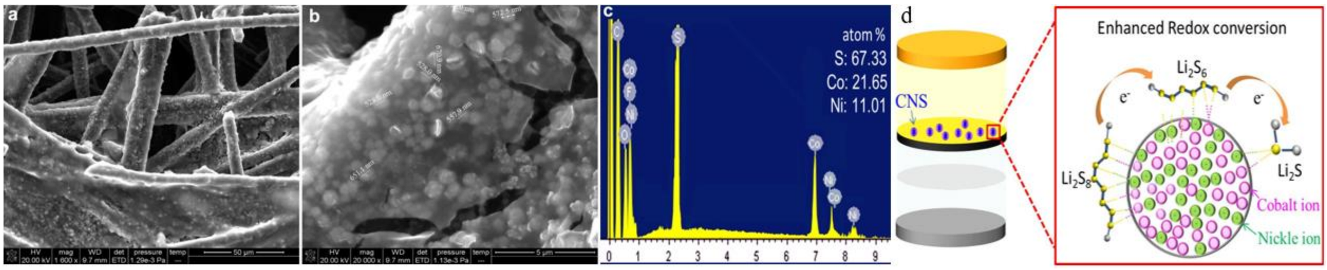

Figure 8 (a-b) SEM images and (c) EDS image of CNS-2/CP electrode after 100 cycles at 0.2C. (d) Schematic illustration of suppression "shuttle effect" with CNS-2/CP separator

4. Conclusion

In summary, regulating bimetallic ratio of Co and Ni, the mixed solvent ratio as well as cobalt source concentration, the as-prepared CNS-2 exhibited strong trapping-capacity towards polysulfides and uniform loading morphology on CP substrate. The introduced cobalt ions played a vital role in the aspects of largely boosting the binding capacity to wards polysulfides of NiS_2. It was found that the lattice distances of bimetallic sulfides CNS-2 are between CoS_2 and NiS_2 along with sole crystal texture as pyrite. CNS-2/CP interlayer with finely efficient catalytic capacity powerfully expedited the bidirectional transformation of S and Li_2S. The enhanced electron transport and ion migration could sustain the comparable electrochemical performances of Li-S batteries with CNS-2/CP interlayer. Higher initial discharge capacity of 1414.4 mAh g^{-1} and 0.35% per cycle of capacity decay was respectively achieved at 0.1C and 0.2C in the condition of 71.8 wt.% sulfur content. In addition, excellent rate performance was still obtained especially at 0.5C and 1C. The cycled CNS-2/CP still remained the morphologic and electrochemical stability. The cationic regulation strategy is regarded as an efficient and feasible approach for designing the pyrite-type electrochemical catalysts for Li-S batteries.

Conflicts of Interest

There are no conflicts to declare.

References

[1] H. J. Zhou, C. L. Song, L. P. Si, X. J. Hong and Y. P. Cai, *Catalysts*, 2020, 10, 9524-9532.

[2] S. Huang, E. Huixiang, Y. Yang, Y. Zhang, M. Ye and C. C. Li, *Journal of Materials Chemistry A*, 2021, 9, 7458-7480.

[3] L. Zhou, D. L. Danilov, R.-A. Eichel and P. H. L. Notten, *Advanced Energy Materials*, 2020, 11, 2001304.

[4] M. Zhao, B.-Q. Li, X.-Q. Zhang, J.-Q. Huang and Q. Zhang, *ACS Central Science*, 2020, 6, 1095-1104.

[5] C. Zhao, G.-L. Xu, T. Zhao and K. Amine, *Angewandte Chemie International Edition*, 2020, 59, 17634-17640.

[6] H. Shin, M. Baek, A. Gupta, K. Char, A. Manthiram and J. W. Choi, *Advanced Energy Materials*, 2020, 10, 2001456.

[7] M. Asif, Z. Ali, H. Qiu, M. Rashad and Y. Hou, *ACS Applied Energy Materials*, 2020, 3, 3541-3552.

[8] S. Nanda and A. Manthiram, *Energy & Environmental Science*, 2020, 13, 2501-2514.

[9] W. G. Lim, S. Kim, C. Jo and J. Lee, *Angewandte Chemie*, 2019, 58, 18746-18757.

[10] S. J. Kim, K. Kim, J. Park and Y. E. Sung, *ChemCatChem*, 2019, 11, 2373-2387.

[11] D. Liu, C. Zhang, G. Zhou, W. Lv, G. Ling, L. Zhi and Q. H. Yang, *Advanced science*, 2018, 5, 1700270.

[12] D. Liu, X. Zhang, Y.-J. Wang, S. Song, L. Cui, H. Fan, X. Qiao and B. Fang, *Nanoscale*, 2020, 12, 9524-9532.

[13] M. Rana, B. Luo, M. R. Kaiser, I. Gentle and R. Knibbe, *Journal of Energy Chemistry*, 2020, 42, 195-209.

[14] Q. Pang, X. Liang, C. Y. Kwok and L. F. Nazar, *Nature Energy*, 2016, 1, 16132.

[15] P. Li, Z. Zhuang, C. Du, D. Xiang, F. Zheng, Z. Zhang, Z. Fang, J. Guo, S. Zhu and W. Chen, *ACS applied materials & interfaces*, 2020, 12, 40194-40203.

[16] K. Liang, K. Marcus, S. Zhang, L. Zhou, Y. Li, S. T. De Oliveira, N. Orlovskaya, Y.-H. Sohn and Y. Yang, *Advanced Energy Materials*, 2017, 7, 1701309.

[17] J. Liu, S. H. Xiao, Z. Zhang, Y. Chen, Y. Xiang, X. Liu, J. S. Chen and P. Chen, *Nanoscale*, 2020, 12, 5114-5124.

[18] S. L. Li, W. F. Zhang, J. F. Zheng, M. Y. Lv, H. Y. Song and L. Du, *Advanced Energy Materials*, 2021, 11, 2000779.

[19] Y. Huang, D. Lv, Z. Zhang, Y. Ding, F. Lai, Q. Wu, H. Wang, Q. Li, Y. Cai and Z. Ma, *Chemical Engineering Journal*, 2020, 387, 124122.

[20] D. Zheng, X.-Q. Yang and D. Qu, *ChemSusChem*, 2016, 9, 2348-2350.

[21] D. Luo, Z. Zhang, G. Li, S. Cheng, S. Li, J. Li, R. Gao, M. Li, S. Sy, Y.-P. Deng, Y. Jiang, Y. Zhu, H. Dou, Y. Hu, A. Yu and Z. Chen, *ACS nano*, 2020, 14, 4849-4860.

[22] J. He, Y. Chen and A. Manthiram, *Advanced Energy Materials*, 2019, 9, 1900584.

[23] S.-H. Chung and A. Manthiram, *Advanced Functional Materials*, 2014, 24, 5299-5306.

[24] P. Han and A. Manthiram, *Journal of Power Sources*, 2017, 369, 87-94.

[25] J. Zhou, X. Liu, J. Zhou, H. Zhao, N. Lin, L. Zhu, Y. Zhu, G. Wang and Y. Qian, *Nanoscale Horizons*, 2019, 4, 182-189.

[26] C. Li, M. Liu, H. Ding, L. He, E. Wang, B. Wang, S. Fan and K. Liu, *Journal of Materials Chemistry A*, 2020, 8, 17527-17536.

[27] X. Yao, H. Cheng, Z. Jiang, Q. Han, Y. Wang and S. Wang, *New Journal of Chemistry*, 2020, 44, 10404-10409.

[28] W. Du, Z. Wang, Z. Zhu, S. Hu, X. Zhu, Y. Shi, H. Pang and X. Qian, *Journal of Materials Chemistry A*, 2014, 2, 9613-9619.

[29] Z. Gao, C. Chen, J. Chang, L. Chen, P. Wang, D. Wu, F. Xu, Y. Guo and K. Jiang, *Electrochimica Acta*, 2018, 281, 394-404.

[30] Q. Wang, F. Gao, B. Xu, F. Cai, F. Zhan, F. Gao and Q. Wang, *Chemical Engineering Journal*, 2017, 327, 387-396.

[31] D. Han, J. Wei, Y. Zhao, Y. Shen, Y. Pan, Y. Wei and L. Mao, *Inorganic Chemistry Frontiers*, 2020, 7, 1428-1436.

[32] C. Liu, H. Ma, M. Yuan, Z. Yu, J. Li, K. Shi, Z. Liang, Y. Yang, T. Zhu, G. Sun, H. Li and S. Ma, *Electrochimica Acta*, 2018, 286, 195-204.

[33] Y. J. Li, S. Y. Lin, D. D. Wang, T. T. Gao, J. W. Song, P. Zhou, Z. K. Xu, Z. H. Yang, N. Xiao and S. J. Guo, *Advanced materials*, 2020, 32, 10.

[34] Z. Shan, Y. He, N. Liu, J. Li, M. Li and Y. Zhang, *Applied Surface Science*, 2021, 539, 148209.

[35] W. Qiu, J. Li, Y. Zhang, G. Kalimuldina and Z. Bakenov, *Nanotechnology*, 2021, 32, 075403.

[36] J. Li, Y. Chen, S. Zhang, W. Xie, S.-M. Xu, G. Wang and M. Shao, *ACS applied materials & interfaces*, 2020, 12, 49519-49529.

[37] J. W. Guo and M. S. Wu, *Electrochimica Acta*, 2019, 327, 10.

[38] W. Ren, L. Xu, L. Zhu, X. Wang, X. Ma and D. Wang, *ACS applied materials & interfaces*, 2018, 10, 11642-11651.

[39] Z. Sun, X. L. Wu, Z. Peng, J. Wang, S. Gan, Y. Zhang, D. Han and L. Niu, *Small*, 2019, 15, e1902491.

[40] J. Xu, W. Zhang, H. Fan, F. Cheng, D. Su and G. Wang, *Nano Energy*, 2018, 51, 73-82.

[41] Y. Men, P. Li, F. Yang, G. Cheng, S. Chen and W. Luo, *Applied Catalysis B: Environmental*, 2019, 253, 21-27.

[42] F. Ma, X. Wang, J. Wang, Y. Tian, J. Liang, Y. Fan, L. Wang, T. Wang, R. Cao, S. Jiao, J. Han, Y. Huang and Q. Li, *Electrochimica Acta*, 2020, 330, 135310.

[43] Q. Yuan, Y. Chen, A. Li, Y. Li, X. Chen, M. Jia and H. Song, *Applied Surface Science*, 2020, 508, 145286.

[44] X. Liao, Z. Li, Q. He, L. Xia, Y. Li, S. Zhu, M. Wang, H. Wang, X. Xu, L. Mai and Y. Zhao, *ACS applied materials & interfaces*, 2020, 12, 9181-9189.

[45] B. Liu, S. Huang, D. Kong, J. Hu and H. Y. Yang, *Journal of Materials Chemistry A*, 2019, 7, 7604-7613.

[46] B. Guo, S. Bandaru, C. Dai, H. Chen, Y. Zhang, Q. Xu, S. Bao, M. Chen and M. Xu, *ACS applied materials & interfaces*, 2018, 10, 43707-43715.

[47] J. Duan, Y. Zou, Z. Li, B. Long and Y. Du, *J. Electroanal. Chem.*, 2019, 847, 113187.

[48] X. Tan, X. Wang, X. Wang, Y. Wang, C. Li and D. Xia, *Ionics*, 2019, 25, 4047-4056.

[49] Z. Li, Z. Ma, Y. Wang, R. Chen, Z. Wu and S. Wang, *Science Bulletin*, 2018, 63, 169-175.

[50] C. Yang, X. Wang, G. Liu, W. Yu, X. Dong and J. Wang, *Journal of Colloid and Interface Science*, 2020, 565, 378-387.

[51] Y.-T. Liu, D.-D. Han, L. Wang, G.-R. Li, S. Liu and X.-P. Gao, *Advanced Energy Materials*, 2019, 9, 1803477.

[52] Z. Shen, M. Cao, Z. Zhang, J. Pu, C. Zhong, J. Li, H. Ma, F. Li, J. Zhu, F. Pan and H. Zhang, *Advanced Functional Materials*, 2020, 30, 1906661.

[53] M. Zhao, H.-J. Peng, Z.-W. Zhang, B.-Q. Li, X. Chen, J. Xie, X. Chen, J.-Y. Wei, Q. Zhang and J.-Q. Huang, *Angewandte Chemie International Edition*, 2019, 58, 3779-3783.

[54] L. Zhang, Z. Chen, N. Dongfang, M. Li, C. Diao, Q. Wu, X. Chi, P. Jiang, Z. Zhao, L. Dong, R. Che, K. P. Loh and H. Lu, *Advanced Energy Materials*, 2018, 8, 1802431.

[55] J. Zhang, Z. Li, Y. Chen, S. Gao and X. W. Lou, *Angewandte Chemie International Edition*, 2018, 57, 10944-10948.

[56] J.-Y. Hwang, H. M. Kim, S. Shin and Y.-K. Sun, *Advanced Functional Materials*, 2018, 28, 1704294.

[57] X. Li, G. Guo, N. Qin, Z. Deng, Z. Lu, D. Shen, X. Zhao, Y. Li, B.-L. Su and H.-E. Wang, *Nanoscale*, 2018, 10, 15505-15512.

[58] C. Y. Zhang, Z. W. Lu, Y. H. Wang, Z. Dai, H. Zhao, G. Z. Sun, W. Lan, X. J. Pan, J. Y. Zhou and E. Q. Xie, *Chemical Engineering Journal*, 2020, 392, 123734.

[59] S. Huang, Y. Wang, J. Hu, Y. Von Lim, D. Kong, L. Guo, Z. Kou, Y. Chen and H. Y. Yang, *NPG Asia Materials*, 2019, 11, 55.

[60] S. Chen, Z. Wu, J. Luo, X. Han, J. Wang, Q. Deng, Z. Zeng and S. Deng, *Electrochimica Acta*, 2019, 312, 109-118.

[61] Z. W. Seh, Y. Sun, Q. Zhang and Y. Cui, *Chemical Society reviews*, 2016, 45, 5605-5634.